Journal of Materials Chemistry A

Enhanced Electrochemical Performance of Hybrid SnO2@MOx (M=Ni, Co, Mn) Core-shell Nanostructures Grown on Flexible Carbon Fibers as the Supercapacitor Electrode Materials

Journal:	*Journal of Materials Chemistry A*
Manuscript ID:	TA-ART-11-2014-006339.R1
Article Type:	Paper
Date Submitted by the Author:	07-Dec-2014
Complete List of Authors:	Liu, Yang; Harbin Normal University, Jiao, Yang; Harbin Normal University, Yin, Bosi; Harbin Normal University, Zhang, Siwen; Harbin Normal University, Qu, Fengyu; Harbin Normal University, Wu, Xiang; Harbin Normal University,

SCHOLARONE™
Manuscripts

Graphical Abstract

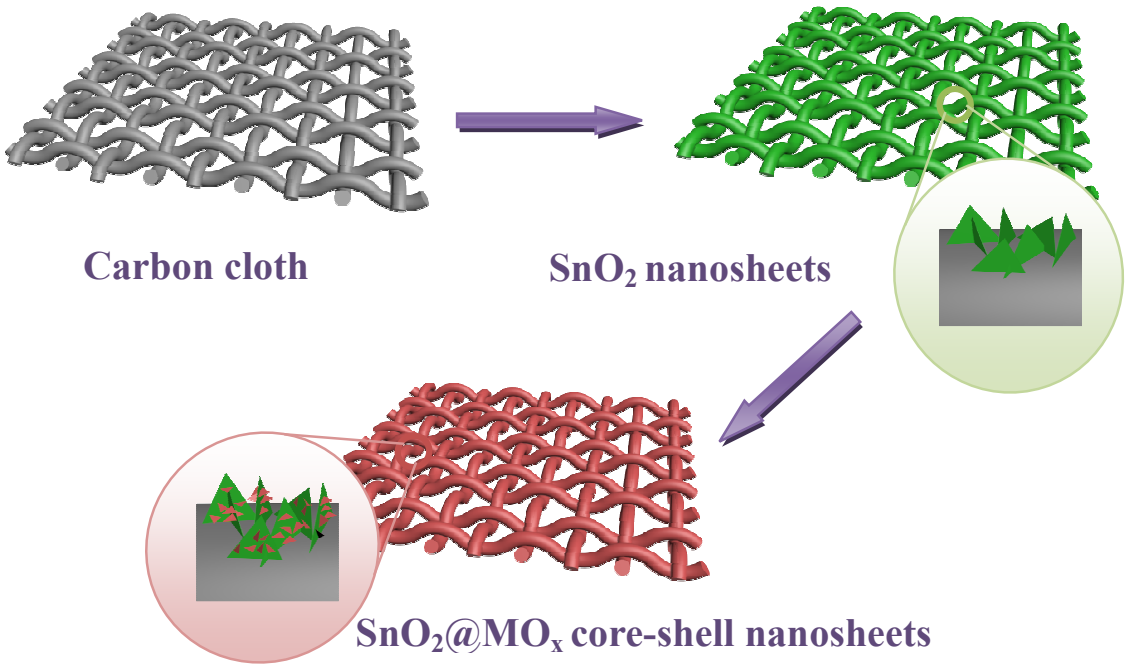

Enhanced Electrochemical Performance of Hybrid $SnO_2@MO_x$ (M=Ni, Co, Mn) Core-shell Nanostructures Grown on Flexible Carbon Fibers as the Supercapacitor Electrode Materials

Yang Liu, Yang Jiao, Bosi Yin, Siwen Zhang, Fengyu Qu, Xiang Wu*

Key Laboratory for Photonic and Electronic Bandgap Materials, Ministry of Education and College of Chemistry and Chemical Engineering, Harbin Normal University, Harbin 150025, P. R. China

*Any correspondences should be addressed: E-mail: wuxiang@hrbnu.edu.cn; wuxiang05@gmail.com

In this paper, hierarchical SnO_2@MOx (SnO_2@NiO, SnO_2@Co_3O_4, SnO_2@MnO_2) heterostructures grown on carbon cloth (CC) for high performance supercapacitors are fabricated by a two-step solution-based method which involves in a hydrothermal process and a chemical bath deposition, which utilizes the better electronic conductivity of SnO_2 nanosheets as the supporting backbone to deposit MOx for supercapacitor electrodes. Particularly, the as-formed SnO_2@MOx heterostructure electrodes showed better electrochemical performance than bare SnO_2 nanosheets. Remarkably, SnO_2@MnO_2 heterostructure electrode showed the highest discharge areal capacitance (980 mF cm^{-2} at 1 mA cm^{-2}), good rate capability (still 767 mF cm^{-2} at 20 mA cm^{-2}), and excellent cycling stability (~21.9% loss after the repetitive 6000 cycles at a charge-discharge current density of 1 mA cm^{-2}). The enhanced pseudocapacitive performance are mainly attributed to its unique hybrid structure, which provides fast ion and electron transfer, a large number of active sites, and good strain accommodation. The excellent electrochemical performance of the as-obtained heterostructure will undoubtedly make these hybrid structures attractive for high performance supercapacitors with high power and energy densities.

1. Introduction

In recent years, with the increasing of energy consumption and environmental pollution problems, great efforts have been devoted to study the alternative energy sources and high power energy storage system. As an important energy storage device with excellent properties of high power density, fast charge-discharge rate, non-pollution and long cycle life, the electrochemical capacitor, also called the supercapacitor (SC), can offer transient but extremely high power, such outstanding advantages make it a good candidate for hybrid electric vehicle, large industrial equipment, and other next generation renewable energy storage application.[1-12] Compare to electric double-layer capacitor (EDLCs), which stores electrical energy by electrostatic accumulation of charges in the electric double-layer near the electrode-electrolyte interfaces, the pseudocapacitors also make use of reversible Faradaic reactions that occurred at the electrode surface, offering much higher specific capacitance than EDLCs.[13-22]

To date, various nanostructures, including transition metal oxides, hybrid composites and conducting polymers, are being widely explored for high performance pseudocapacitors because of their low cost, low toxicity and great flexibility in structure and morphology.[23-28] Among those transition metal oxides, RuO_2 and hydroxides show the best performance.[14, 29-31] However, their expensive nature limits their practical use. At the same time, transition metal oxides suffer from poor conductivity. Therefore, to meet the requirement of high specific capacitance,

structural stability and boost the electrochemical utilization of active materials, an effective approach is to design hybrid nanoheteroarchitectures.

As known, surface area of the nanosheet is much higher than that of the nanowire. In addition, the interconnected sheet networks make the electrode much stable toward cycling. Based on the above consideration, we design a novel hybrid SnO_2@MOx heterostructure via a two-step solution route. Ultrathin SnO_2 nanosheets uniformly grown on carbon cloth were used as the backbone to support and provide reliable electrical connection to MOx coatings with surface areas accessible to electrolyte, enabling fully utilization of MOx and fast electronic and ionic conduction through the electrode. Impressively, compared with bare SnO_2 nanosheets electrode, SnO_2@MOx hybrid electrodes show prominent electrochemical performance with higher capacitance as well as better cycling stability.

2. Experimental Sections

2.1 Material synthesis

Synthesis of SnO_2 nanosheets: All chemicals were used without any further purification. Prior to the synthesis, a piece of CC (1 cm × 1 cm) was cleaned by acetone, ethanol, and distilled water in sequence. In a typical synthesis, 2.5 mmol of $SnCl_2 \cdot 2H_2O$, 5.0 mmol of $C_6H_5Na_3O_7 \cdot 2H_2O$ were dissolved in 40 mL of an ethanol-water (1:1) solution at room temperature. After stirring for 60 min, the homogeneous solution was transferred into a 50 mL autoclave and clean carbon cloth was immersed into the solution around autoclave wall. Then the autoclave was sealed and heated at 180 ^{o}C for 8 h in an electric oven. When the autoclave was cooled to

room temperature, CC coated with brown precursor was taken out and washed with DI water. Finally, the precursor on CC was annealed at 400 ^{o}C for 2 h in air.

Synthesis of SnO_2@Co_3O_4: 2 mmol $Co(NO_3)_2 \cdot 6H_2O$, 8 mmol NH_4F and 10 mmol urea were dissolved in 36 mL distilled water and stirred to form a clear solution, then transferred to a 50 mL pyrex beaker. Subsequently, carbon cloth coated SnO_2 nanosheets was placed in the beaker vertically and maintained at 100 ^{o}C for 1 h, and then allowed to cool to room temperature naturally. SnO_2@Co_3O_4 composite was rinsed several times with distilled water and ethanol with the assistance of ultrasonication, and dried at 80 ^{o}C for 6 h, finally annealed at 300 °C for 2 h in air.

Synthesis of SnO_2@NiO: carbon cloth coated SnO_2 nanosheets were placed vertically in a 250 mL pyrex beaker. Solution was prepared by adding 20 mL of aqueous ammonia (25-28%) to the mixture of 100 mL of 1 M nickel sulfate and 80 mL of 0.25 M potassium persulfate. Immersing into the solution for 10 min at 20 ^{o}C, carbon cloth was taken out and rinsed with distilled water. Then the sample was annealed at 350 ^{o}C for 1 h in air..

Synthesis of SnO_2@MnO_2: A piece of SnO_2 CC was soaked in a 50 mL solution containing 5 mmol of $KMnO_4$, 5 mmol of H_2SO_4 and 50 mL of deionized water. Carbon cloth with SnO_2 nanosheets was immersed into the solution, which was kept at 85 °C in an electric oven. The duration of immersion was 60 min. Next, the sample was rinsed with deionized water and subsequently annealed at 400 °C for 5 min in air.

2.2 Characterization

The microstructure of the samples was investigated by powder X-ray diffraction

system (XRD, Rigaku Dmax-2600/pc) equipped with Cu Kα radiation (λ=0.1542 nm), scanning electron microscopy (FESEM; Hitachi-S4800) and transmission electron microscopy (TEM; JEOL-2010). X-ray photoelectron spectroscopy (XPS) was measured on a Perkin-Elmer model PHI 5600 XPS system.

2.3 Electrochemical measurements

Cyclic voltammetry (CV) curves, galvanostatic charge-discharge and electrochemical impedance spectroscopy (EIS) tests were carried out using a classical three-electrode configuration in 1 M Na_2SO_4 aqueous electrolyte (for SnO_2 and SnO_2@MnO_2) and 1 M KOH aqueous electrolyte (for SnO_2@NiO and SnO_2@Co_3O_4) on a CHI 660E electrochemical workstation. Cyclic voltammetry curves were measured in a potential range between 0 and -0.8 V at different scan rates, and the charge/discharge processes were performed by cycling the potential from 0 to -0.8 V at different current densities. CC supported nanostructures (1 cm^2 area) act directly as the working electrodes. A Pt plate and Ag/AgCl were used as the counter electrode and the reference electrode, respectively. All potentials were referred to the reference electrode. The specific capacitance (mF cm^{-2}) and current density (mA cm^{-2}) were calculated based on the mass of four active materials. And the small contribution from CC was subtracted. The specific capacitance is calculated by $C = It/(\Delta V\ S)$, where I is discharge current, t is discharge time, S is the geometrical area of the electrode, and ΔV is the voltage drop upon discharging. Electrochemical impedance spectroscopy (EIS) measurements were carried out by applying an AC voltage with 1 mV amplitude in a frequency range from 0.1 Hz to 100 kHz at open circuit potential. The

cyclic stability was evaluated by cyclic voltammetry measurements at a current density of 1 mA cm^{-2} for 6000 cycles.

3. Results and discussion

Fig. 1 illustrates two-step synthesis route of $SnO_2@MO_X$ heterostructures by combining a hydrothermal synthesis and a chemical bath deposition method. Hydrothermally grown SnO_2 nanosheets serve as the backbone for the subsequent deposition of MOx nanosheets.

The morphologies of SnO_2 nanosheets on CC are investigated firstly by FESEM. It can be seen that SnO_2 sample composed of many 1D nanosheets, which arrange uniformly and perpendicular to CC after hydrothermal process, it is worth mentioning that the nanosheets connect with each other, forming the network and making the structure more stably, as shown in Fig. 2a-b. The formation of the nanosheets array is based on heterogeneous nucleation and growth due to the lower interfacial nucleation energy on the substrate. The enlarged view in Fig. 2c shows that the surface of SnO_2 nanosheet is extremely smooth. Besides, the nanosheets are ultrathin with average thickness of about only 10 nm which can do benefit to the fully utilization of active materials. The microstructure of single nanosheet is also investigated by TEM. Fig. 2d shows a low TEM image of a single SnO_2 nanosheet, which is consistent with the SEM results. High resolution TEM (HRTEM) image in Fig. 2e shows the clear lattice spacings of 0.337 nm and 0.265 nm, corresponding to the interplanar distances of (110) and (101) plane of rutile SnO_2, respectively. The inset in Fig. 2e exhibits a typical SAED pattern, which confirmed that the prepared nanosheets are single crystal

structure. The crystal phases of the as-prepared SnO_2 nanosheets was studied by using X-ray diffraction (XRD) and the corresponding results are presented in Fig. 2f. Except the peak marked with the square, which comes from carbon template, all other peaks agree well with tetragonal rutile SnO_2 phase (JCPDS Card, No. 41-1449).

To better understand the formation process of SnO_2 nanosheets, time dependent experiments were conducted as depicted in Fig. S1. When reaction time is only 2 h, a plenty of tiny particles were attached on the surface of CC. As reaction time prolongs to 4 h, irregular aggregates with sheet-like subunits are formed. With reaction time increasing to 6 h, the nanosheets become more pronounced. After reaction time is 8 h, well-defined SnO_2 nanosheet arrays were obtained.

SnO_2 nanosheet grown on CC is an ideal scaffold to form electroactive SnO_2@MOx composites so as to improve the electrochemical capacitor properties. Fig. 3 shows SEM and TEM images of the composites, in which three electroactive materials were deposited on SnO_2 nanosheets, respectively. As can be seen from Fig. 3a, d and g, the fluffy MOx nanosheet "shells" covered uniformly on SnO_2 nanosheet "core" to form unique core-shell structures. High magnification SEM images are shown in Fig. 3b, e and h. respectively. Although MO_x "shells" are ultrathin and interconnected, they do not fully coat the whole SnO_2 core, which make the inner SnO_2 nanosheets accessible to the electrolyte as well. Moreover, it is worth noting that in all three cases the inner SnO_2 nanosheets remain interlaced with each other to align vertically on the substrate, which can benefit the transportation of electrons and the integrity of the structure. Further observation by HRTEM (Fig. 3c, f and i) reveals that

MOx nanosheets can be easily distinguished from SnO_2 nanosheets. Selected area electron diffraction (SAED) pattern of the composite materials confirmed that the prepared heterostructures are polycrystalline structure, as shown in the inset in Fig. 3c, f and i.

The structure and composition information of SnO_2@MOx composites were conducted by X-ray photoelectron spectroscopy (XPS) measurement and the results are shown in Fig. 4. In regard to Co 2p peak in Fig. 4a, it contains a low energy band (Co $2p_{3/2}$) and a high energy band (Co $2p_{1/2}$) at 781.3 and 796.8 eV, which is consistent with the results reported elsewhere.[32] The spin-orbit splitting value of Co $2p_{1/2}$ and Co $2p_{3/2}$ is over 15 eV, suggesting the coexistence of Co^{2+} and Co^{3+}.[33, 34]

In Fig. 4b, energy bands of Ni $2p_{1/2}$ and Ni $2p_{3/2}$ shift to 873.2 and 855.7 eV, respectively. Main Ni $2p_{3/2}$ peaks is close to 854.9 eV for Ni^{2+} but much lower than 857.1 eV for Ni^{3+},[35, 36] suggesting that it is in the divalent state. However, possible existence of trivalent Ni cannot be excluded. In SnO_2@MnO_X composite, broad peaks of Mn $2p_{3/2}$ and $2p_{1/2}$ are located around 642.3 and 653.8 eV, respectively, demonstrating Mn^{4+} ions were dominant in the products.[37,38] In addition, the difference of the peak separation between Mn $2p_{3/2}$ and $2p_{1/2}$ is about 11.5 eV, further proving the above statement. Since binding energy difference of Mn $2p_{3/2}$ and $2p_{1/2}$ can be used to indicate the oxidation state of Mn.[38] In O 1s spectra, the peak at 532.3 eV could be ascribed to M-O (M= Co Ni and Mn), respectively. The above results reveal that the electroactive materials (NiO, Co_3O_4 and MnO_2) were successfully deposited on SnO_2 nanosheets.

X-ray diffraction patterns of SnO_2@Co_3O_4, SnO_2@NiO and SnO_2@MnO_2 heterostructures are almost the same as that of SnO_2 (Fig. S2), it is because that the diffraction peaks of NiO, Co_3O_4, and MnO_2 are so weak that it is difficult to be detected.

To investigate the capacitive performance of the as-prepared products, the pseudocapacitors based on SnO_2 and MO_x@SnO_2 nanosheets are fabricated. Fig. 5a compares the cyclic voltammetry (CV) curves of bare SnO_2, SnO_2@Co_3O_4, SnO_2@NiO and SnO_2@MnO_2 nanosheets and pure CC at a scan rate of 10 mV s^{-1} in a potential window of 0 to -0.8 V. Remarkably, the area integration of SnO_2@MO_x within the current-voltage curve is much larger than that of the bare one, indicating that heterostructured nanosheet arrays possess higher electrochemical reaction activity. It could be attributed to the additional pseudocapacitance from MO_x. To check the effect of substrate, CV curve of CC was also shown. We can find that the integrated electrode exhibits much higher capacitive current density than that of pure CC, which reveals that the substrate effect of CC can be neglected in all cases due to its small contribution to the total capacitance of the electrodes. More representative CV curves of bare SnO_2 and SnO_2@MO_x composite electrodes at different scan rates are shown in Fig. S3. CV curves of SnO_2@Co_3O_4 and SnO_2@NiO are different from ideal rectangular shape of typical electric double-layer capacitance. SnO_2, Co_3O_4 and NiO have a couple of redox peaks, respectively. Moreover, it is found that the redox currents increase upon when increasing the scan rates. Meanwhile the anodic and cathodic peaks shift toward the positive and negative potentials, revealing low

resistance of the electrodes and fast ionic and electronic transport rate between the active materials and CC substrate,[39] which can be further confirmed by electrochemical impedance spectroscopy (EIS, Fig. 6). Fig. 5b shows typical charge-discharge curves (CC curves) of three electrodes at a current density of 1 mA cm^{-2}. Evidently, the heterostructured composites possess much longer discharge times than bare SnO_2 nanosheets (470 s, 528 s and 783 s for the SnO_2@Co_3O_4, SnO_2@NiO and SnO_2@MnO_2, respectively, and 315 s for bare SnO_2 nanosheets). Moreover, four electrodes were also tested under different current densities of 1, 2, 5, 10 and 20 mA cm^{-2}, as shown in Fig. S4. It is noted that the curves of SnO_2 and SnO_2@MnO_2 are symmetrical, suggesting good electrochemical capacitive characteristics. In CC curves of SnO2@Co3O4, a linear variation from −0.4 to -0.8 V indicates the EDLC behavior, and the weak sloped variation above -0.3 V indicates the pseudocapacitive nature of Co3O4. Analogously, in CC curve of SnO2@NiO, a linear variation from −0.3 to -0.8V can be observed, and the sloped variation above -0.2 V corresponding to the peaks in CV curves. Since SnO2 has not been completely covered by MOx, it would make a contribution to the capacitance, thus charging and discharging behavior of Co_3O_4 and NiO can be affected by SnO_2, and the voltage plateaus in CC curve of SnO_2@Co_3O_4 and SnO_2@NiO are not significant, the inconspicuous voltage plateaus corresponding to these weak peaks in CV curves.

Based on the charge-discharge curves of these materials, the summary plots of areal capacitances vs. current densities are shown in Fig. 5c. With the current density increasing from 1 to 20 mA cm^{-2}, SnO_2@Co_3O_4, SnO_2@NiO and SnO_2@MnO_2

exhibit 58.9, 57.4 and 63.8% retention of their initial capacitance, which is much higher than that of SnO_2 nanosheets (~50.7%). This reveals that $SnO_2@MO_x$ possess high rate capability even at such a high current density of 20 mA cm^{-2}. Such a good rate capability of $SnO_2@MnO_2$ could be attributed to unique structure characteristics such as ultrathin MO_x nanosheets covering on the surface of SnO_2 nanosheets, resulting in the short paths for electron transport and species diffusion, as well as synergetic effect from SnO_2 and MO_x materials during the charge-discharge process.

A good cycling stability is crucial for a real supercapacitor. The as-prepared products are subjected to continuous galvanostatic charge-discharge measurements at a current density of 1 mA cm^{-2}. As shown in Fig. 5d, all of hybrid structure electrodes exhibit an increase at first due to gradual activation of the electrode.[40,41] After 6000 cycles, $SnO_2@Co_3O_4$, $SnO_2@NiO$ and $SnO_2@MnO_2$ electrodes can maintain 58.3, 63.8 and 78.1% of its initial SC, respectively. While for SnO_2 electrode, the SC of the 6000^{th} cycle retained only 47.2 %, which is much lower than $SnO_2@MO_x$ eletrodes. The comparison of electron conductivity for SnO_2 and $SnO_2@MO_x$ eletrodes can be seen from the EIS results (Fig. 6). The EIS results demonstrate that the charge transfer resistances of $SnO_2@Co_3O_4$, $SnO_2@NiO$ and $SnO_2@MnO_2$ electrodes are 2.6, 1.7 and 0.8 Ω, which is much smaller than that of SnO_2 electrode (3.8 Ω), demonstrating that the as-prepared $SnO_2@MO_x$ supercapacitors possess a relatively good stability than bare SnO_2.

The enhancement mechanism of pseudocapacitive performance of $SnO_2@MO_x$ core-shell nanosheet arrays could be explained as follow: First, the core-shell

structured materials possess good pseudocapacitive behavior, which contributes the total electrochemical charge storage. Second, large open nanoarchitecture of nanosheets could ensure a high utilization of the electrode materials and fast electrolyte irrigation. In combination with the good conductivity of SnO_2 core, high areal capacitance and a good rate capability can be expected. Third, SnO_2 nanosheets connect with each other, forming a flake network. These nanosheets support with each other, making the structure more stably. Such a stable and connecting structure helps to alleviate the structure damage caused by volume expansion during the cycling process, resulting in an enhanced stability. Fourth, MO_x nanosheet shells are well wrapped on the surface of SnO_2 nanosheets core. It could provide facile electron transport for Faradic reaction and maintain the structural integrity of the core during charge-discharge process. Finally, MO_x nanosheet shells are interconnected but still do not fully cover the whole SnO_2 core. Even the core SnO_2 nanosheets are highly accessible to electrolyte for energy storage. Therefore, nearly all the core-shell nanosheets are highly accessible to electrolyte to obtain a high areal capacitance. Moreover, as both the “core” and the “shell” are ultrathin, the electrolyte can easily diffuse into the underneath part of the electrode materials, so all the active materials can participate in the electrochemical charge storage process, leading to a higher areal capacitance.

4. Conclusions

In summary, hybrid SnO_2@MOx core-shell heterostructures are prepared by a facile and high efficient solution-based method. SnO_2@MOx core-shell nanosheets

array electrodes exhibit excellent pseudocapacitive behaviors with high areal capacitance and good cycling stability, making it excellent electrode materials for high-performance supercapacitors. Its outstanding electrochemical performance comes from the unique core/shell configuration, which provides fast ion and electron transfer, large number of active sites and good strain accommodation.

Acknowledgement

This work was supported by the Scientific Research Fund of Heilongjiang Provincial Education Department (12531179) and Program for Scientific and Technological Innovation Team Construction in Universities of Heilongjiang (No. 2011TD010).

References

1 P. H. Yang, Y. Ding, Z. Y. Lin, Z. W. Chen, Y. Z. Li, P. F. Qiang, M. Ebrahimi, W. J. Mai, C. P. Wong and Z. L. Wang, *Nano Lett*., 2014, **14**,731-736.

2 J. P. Liu, J. Jiang, M. Bosman, H. J. Fan, *J. Mater. Chem.* 2012, **22**, 2419-2426.

3 Y. Jiao, Y. Liu, B. S. Yin, S. W. Zhang , F. Y. Qu, X. Wu, *Nano Energy*, 2014, **10**, 90-98.

4 X. H. Xia, D. L. Chao, Z. X. Fan, C. Guan, X. H. Cao, H. Zhang and H. J. Fan, *Nano Lett*., 2014, **14**, 1651-1658.

5 B. Cui, H. Lin, J. B. Li, X. Li, J. Yang, J. Tao, *Adv. Funct. Mater.*, 2008, **18**, 1440-1447.

6 D. W. Choi, G. E. Blomgren, P. N. Kumta, *Adv. Mater.*, 2006, **18**, 1178-1182.

7 P. Simon and Y. Gogotsi, *Nat. Mater.*, 2008, **7**, 845-854.

8 M. S. Dresselhaus, I. L. Thomas, *Nature*, 2001, **414**, 332-337.

9 J. R. Miller, P. Simon, *Science*, 2008, **321**, 651-652.

10 P. J. Hall, M. Mirzaeian, S. I. Fletcher, F. B. Sillars, A. J. R. Rennie, G. O. Shitta-Bey, G. Wilson, A. Cruden, R. Carter, *Energy. Environ. Sci.*, 2010, **3**, 1238-1251.

11 G. Q. Zhang, H. B. Wu, H. E. Hoster, M. B. Chan-Park and X. W. Lou, Energy Environ. Sci., 2012, **5**, 9453-9456.

12 C. Guan, X. H. Xia, N. Meng, Z. Y. Zeng, X. H. Cao, C. Soci, H. Zhang and H. J. Fan, *Energy Environ. Sci.*, 2012, **5**, 9085-9090.

13 J. Chmiola, G. Yushin, Y. Gogotsi, C. Portet, P. Simon and P. L. Taberna, *Science*, 2006, **313**, 1760-1763.

14 S. Sarangapani, B. V. Tilak, C. P. Chen, *J. Electrochem. Soc.*, 1996, **143**, 3791-3799.

15 C. Guan, X. L. Li, Z. L. Wang, X. H. Cao, C. Soci, H. Zhang and H. J. Fan, *Adv. Mater.*, 2012, **24**, 4186-4190.

16 J. P. Liu, J. Jiang, C. W. Cheng, H. X. Li, J. X. Zhang, H. Gong and H. J. Fan, *Adv. Mater.*, 2011, **23**, 2076-2081.

17 C. C. Hu, K, H. Chang, M. C. Lin and Y. T. Wu, *Nano Lett.*, 2006, **6**, 2690-2695.

18 S. C. Pang, M. A. Anderson, and T. W. Chapmanb, *J. Electrochem. Soc.*, 2000, **147**, 444-450.

19 Q. T. Qu, Y. Li, L. L. Shi, W. L. Guo, Y. P.Wu, H. P. Zhang, S. Y. Guan, and R. Holze, *Electrochem. Commun.*, 2009, **11**, 1325-1328.

20 C. L. Chen, D. L. Zhao, D. Xua and X. Wang, *Mater. Chem. Phys.*, 2006, **95**, 84-88.

21 X. P. Zhou, H. Y. Chen, D. Shu, C. He and J. M. Nan, *J. Phys. Chem. Solids*, 2009, **70**, 495-500.

22 Y. G. Wang, H. Q. Li and Y. Y. Xia, *Adv. Mater.*, 2006, **18**, 2619-2623.

23 P. H. Yang and W. J. Mai, *Nano Energy*, 2014, **8**, 274-290.

24 L. N. Gao, X. F. Wang, Z. Xie, W. F. Song, L. J. Wang, X. Wu, F. Y. Qu, D. Chen, G. S. Shen, *Journal of Materials Chemistry A*, 2013, **1**, 7168-7173.

25 C. Guan, J. P. Liu, C. W. Cheng, H. X. Li, X. L. Li, W. W. Zhou, H. Zhang and H. J. Fan, *Energy Environ. Sci.*, 2011, **4**, 4496-4499.

26 P. H. Yang, Y. Z. Li, Z. Y. Lin, Y. Ding, S. Yue, C. P. Wong, X. Cai, S. Z. Tan and W. J. Mai, *J. Mater. Chem. A*, 2014, **2**, 595-599.

27 Y. Liu, Y. Jiao, Z. L. Zhang, F. Y. Qu, A. Umar and X. Wu, *ACS Appl. Mater. Interfaces*, 2014, **6**, 2174-2184.

28 W. W. Zhou, D. Z. Kong, X. T. Jia, C. Y. Ding, C. W. Cheng and G. W. Wen, *J. Mater. Chem. A*, 2014, **2**, 6310-6315.

29 R. R. Bi, X. L. Wu, F. F. Cao, L. Y. Jiang, Y. G. Guo, L. J. Wan, *J. Phys. Chem. C*, 2010, **114**, 2448-2451.

30 J. P. Zheng, P. J. Cygan and T. R.Jow, *J. Electrochem. Soc.*, 1995, **142**, 2699-2703.

31 C. C. Hu, K. H. Chang, M. C. Lin and Y. T. Wu, *Nano Lett.*, 2006, **6**, 2690-2695.

32 L. H. Bao, J. F. Zang and X. D. Li, *Nano Lett.*, 2011, **11**, 1215-1220.

33 B. Ernst, S. Libs, P. Chaumette and A.Kiennemann, *Appl. Catal. A*, 1999, **186**, 145-168.

34 J. Xu, P. Gao, T. S. Zhao, *Energy Environ. Sci*. 2012, **5**, 5333-5339.

35 M. Oku, K. Hirokawa, *J. Solid State Chem.*, 1979, **30**, 45-53.

36 M. W. Nydegger, G. Couderc, M. A. Langell, *Appl. Surf. Sci*., 1999, **147**, 58-66.

37 M. Toupin, T. Brousse, D. Belanger, *Chem. Mater.*, 2004, **16**, 3184-3190.

38 M. Chigane, M. Ishikawa, *J. Electrochem. Soc.*, 2000, **147**, 2246-2251.

39 Y. Chen, B. Qu, L. Hu, Z. Xu, Q. Li and T. Wang, *Nanoscale*, 2013, **5**, 9812-9820.

40 X. Liu, S. Shi, Q. Xiong, L. Li, Y. Zhang, H. Tang, C. Gu, X. Wang and J. Tu, ACS *Appl. Mater. Interfaces*, 2013, **5**, 8790-8795.

41 C. Yuan, J. Li, L. Hou, J. Lin, X. Zhang and S. Xiong, *J. Mater. Chem. A*, 2013, **1**, 11145-11151.

Figure captions

Figure 1. Nanofabrication flowchart of hierarchically structured composite electrode.

Figure 2. (a-e) SEM and TEM images of SnO_2 nanosheet arrays grown on the carbon cloth. (f) Typical XRD patterns of the prepared SnO_2.

Figure 3. SEM and TEM images of the (a-d), $SnO_2@Co_3O_4$, (e-h), $SnO_2@NiO$, (i-l), $SnO_2@MnO_2$ composites.

Figure 4. XPS spectra of the (a) Co 2p, (b) Ni 2p, (c) Mn 2p, (d) O 1s.

Figure 5. (a) CV curves of CC, SnO_2 and $SnO_2@MO_x$ nanosheet arrays at a scan rate of 10 mV s^{-1}.(b) The galvanostatic charge-discharge curves of SnO_2 and $SnO_2@MO_x$ nanosheet arrays electrodes. (c) A comparison of areal capacitances for SnO_2 and $SnO_2@MO_x$ nanosheet arrays electrodes as a function of the current density, respectively. (d) Cycling performance of the SnO_2 and $SnO_2@MO_x$ hybrid electrodes

Figure 6. EIS Nyquist plots of SnO_2, $SnO_2@Co_3O_4$ $SnO_2@NiO$ and $SnO_2@MnO_2$ composites.

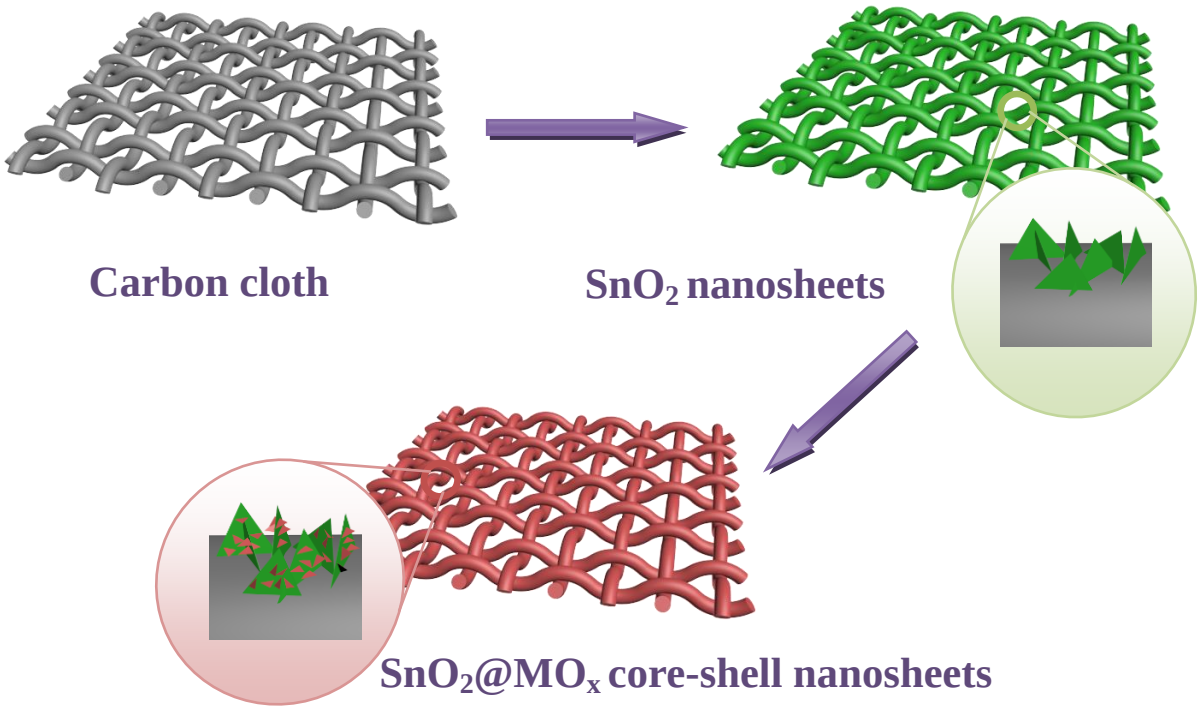

Fig. 1 Yang Liu et al.

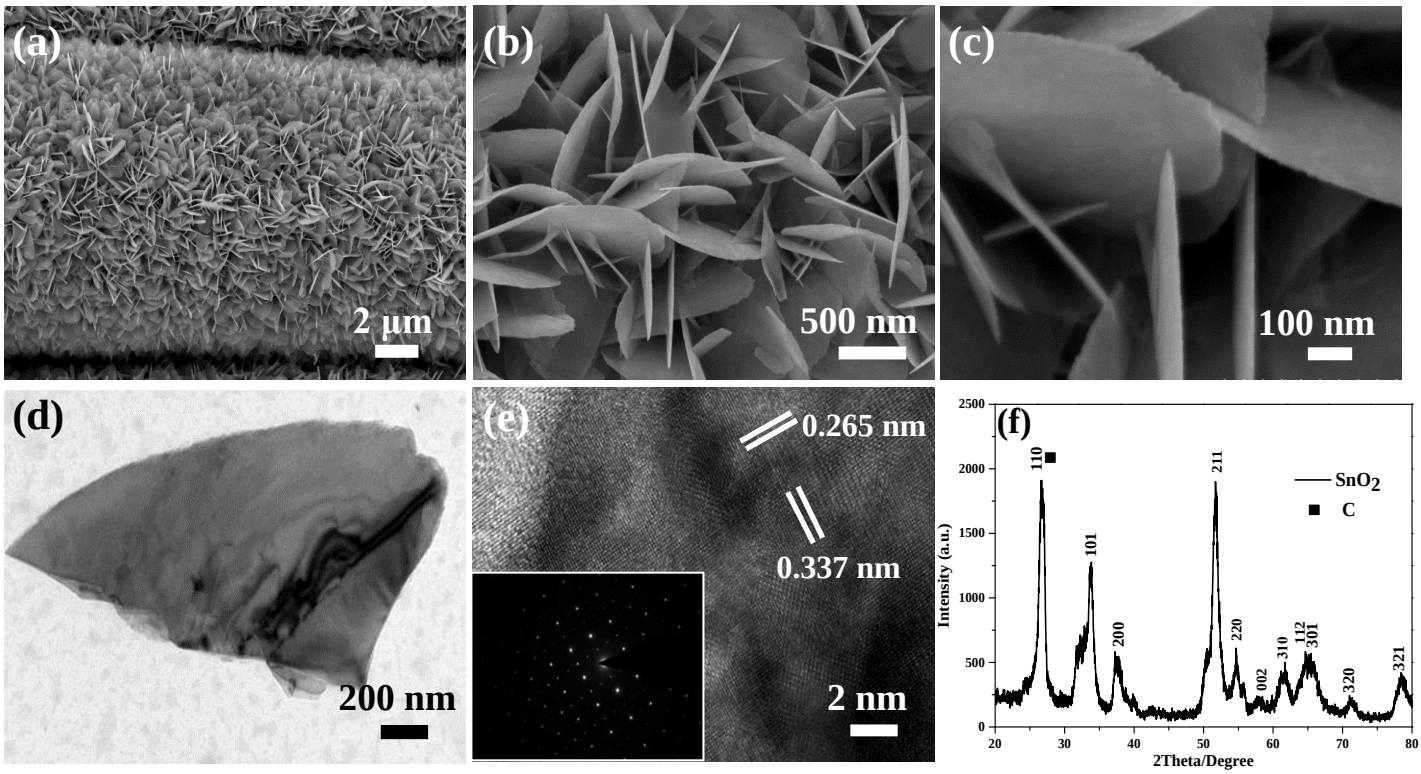

Fig. 2 Yang Liu et al.

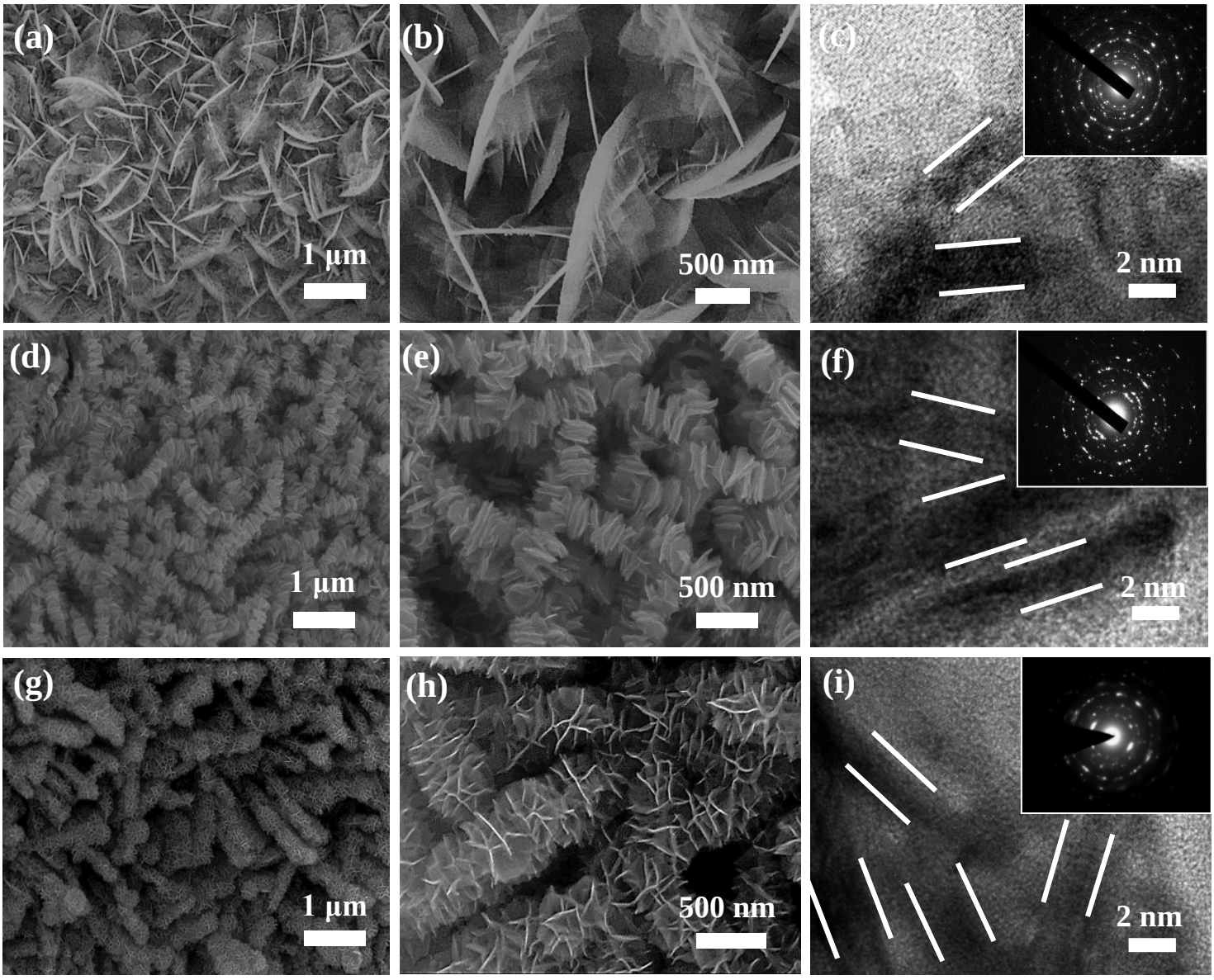

Fig. 3 Yang Liu et al.

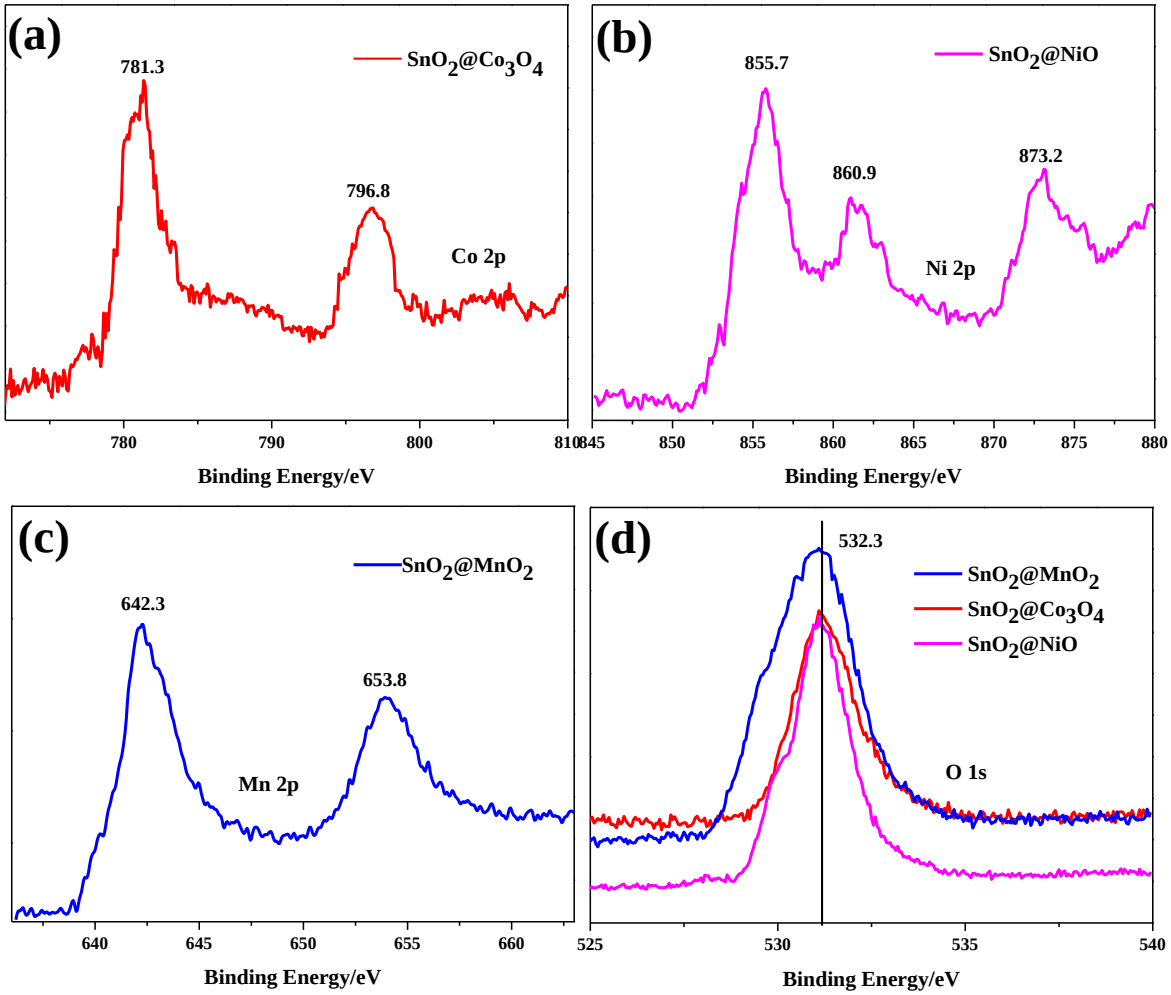

Fig. 4 Yang Liu et al.

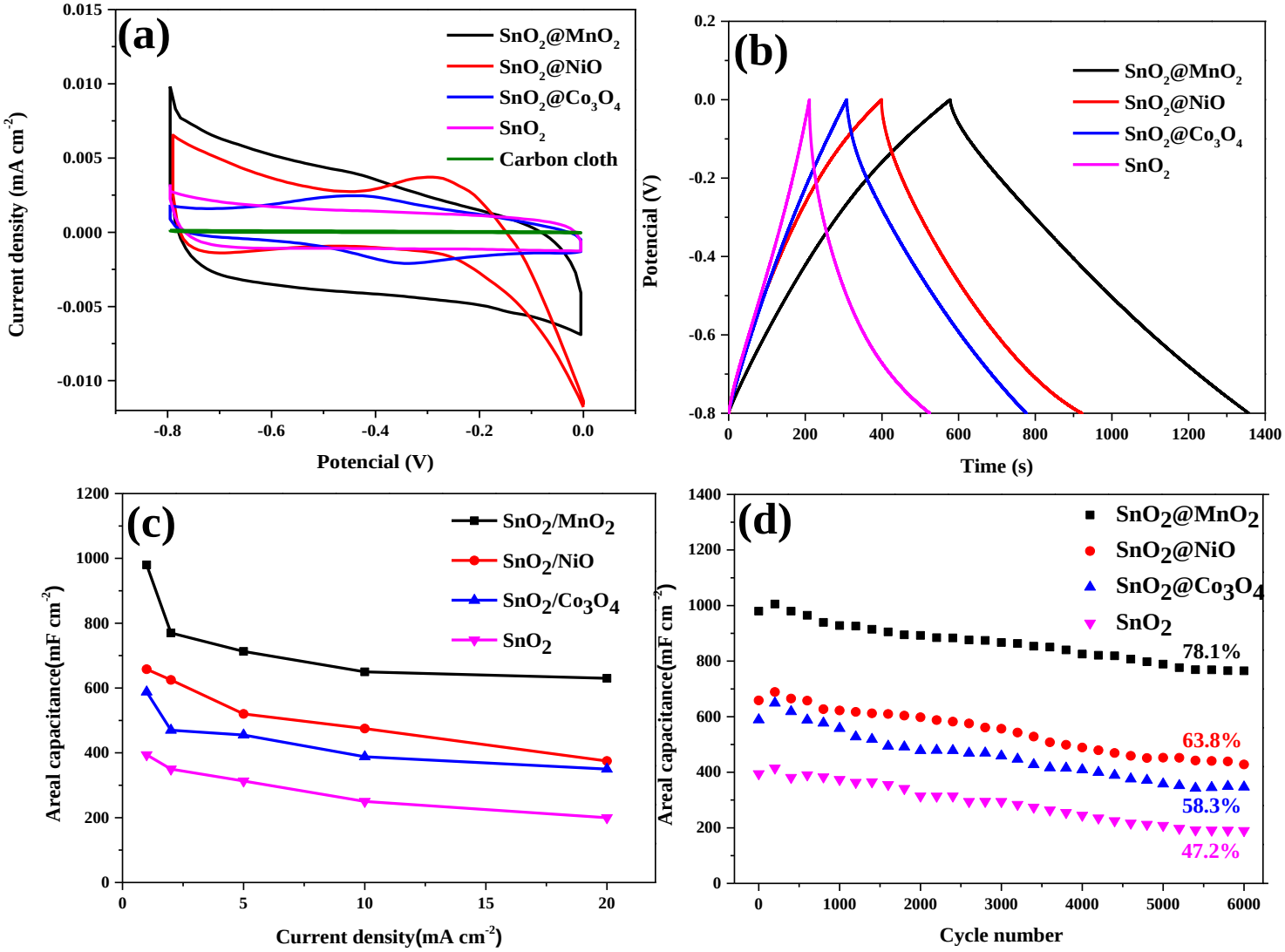

Fig. 5 Yang Liu et al.

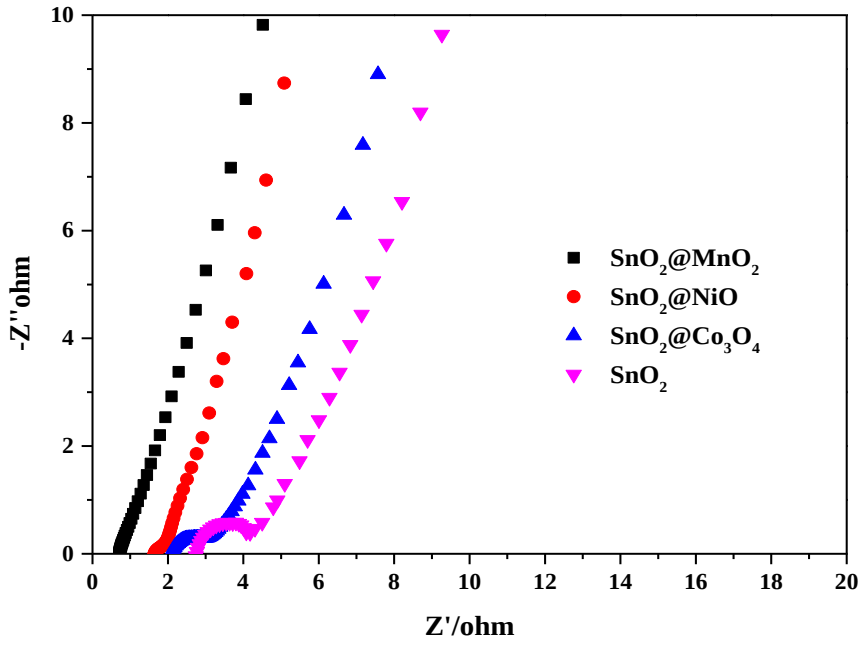

Fig.6 Yang Liu et al.